ORIGINAL PAPER

Partially carbonized tungsten oxide as electrode material for asymmetric supercapacitors

Hem Kanwar Rathore[1] · Muruganandham Hariram[1] · Kamlendra Awasthi[1] · Manoj Kumar[1] · Debasish Sarkar[1] · Mukhesh K. Ganesha[2] · Ashutosh K. Singh[2] · Debanjan Das[3] · Ashok Shukla[4]

Abstract

Synthesis of partially carbonized tungsten oxide employing a simple, one-step, and scalable in-situ reduction/carbonization process is reported along with its electrochemical performance as electrode material in an asymmetric supercapacitor. The synthesis produces a WO_2/W_2C composite where the carbide part is introduced to enhance the electronic conductivity of redox-active tungsten oxide. Electrochemical performance and charge storage mechanism of WO_2/W_2C heterostructure is elucidated in detail. The electrode material exhibits compelling areal capacitance within -0.3 to -1 V window in half-cell configuration. Notably, both surface-controlled and diffusion-controlled processes govern the charge storage behavior, with the former dominating at higher scan rates. An asymmetric supercapacitor assembled with WO_2/W_2C composite as a negative electrode and activated charcoal (AC) as a positive electrode exhibits good cycling stability within a stable voltage window of 0.2 to 1.4 V and could deliver an energy density of 0.6 mWh/cm^3 at a power density of 9 mW/cm^3 in aqueous electrolyte. This study thus provides a fundamental understanding of the charge storage mechanism in WO_2/W_2C composite electrode which is required for realizing futuristic energy storage devices with low cost but efficient electroactive materials.

Keywords Partially carbonized tungsten oxide · Composite heterostructures · Charge-storage mechanism · Surface-controlled redox capacitance · Aqueous asymmetric supercapacitor

Introduction

Rapid exhaustion of fossil fuels, climate change, and rising environmental concerns necessitate to adopt renewable and clean energy resources to cope with the increasing energy demand and relieve environmental crisis [1]. However, storing and retrieving renewable energy remains an obstacle due to its sporadic nature [2]. In this regard, concerns for novel high-performance energy storage devices are growing among which supercapacitors (SCs) are promising option due to their high power density than conventional batteries and high energy density than regular capacitors [3, 4]. Moreover, the excellent cycle life, fast charge–discharge, low maintenance cost, and high reliability of supercapacitors are additional advantages over batteries. But the limited energy density of SCs is restricting their widespread applications [2–5]. Accordingly, the current challenge of the research community is to increase energy density of supercapacitors without affecting their power density and cycle life. The energy density, as per the equation $E = \frac{1}{2}CV^2$, can be enhanced either by increasing the capacitance value or by extending cell voltage [6]. Capacitance of SCs can be improved by employing nanostructured pseudocapacitive electrode materials with fast redox activity [7]. On the other hand, assembling asymmetric supercapacitors (ASCs) can widen the cell voltage by utilizing complementary voltage windows of individual

Hem Kanwar Rathore and Muruganandham Hariram contributed equally to this work

✉ Debasish Sarkar
  deb.sarkar1985@gmail.com; debasish.phy@mnit.ac.in

✉ Ashok Shukla
  akshukla2006@gmail.com

[1] Department of Physics, Malaviya National Institute of Technology Jaipur, Jaipur, Rajasthan 302017, India

[2] Centre for Nano and Soft Matter Sciences, Bengaluru 562162, India

[3] Analytical Chemistry and Center for Electrochemical Sciences, Ruhr-University Bochum, Bochum 44780, Germany

[4] Solid State and Structural Chemistry Unit, Indian Institute of Science, Bengaluru 560012, India

electrode materials, and hence considerably increase their energy density [8]. From this perspective, designing novel pseudocapacitive electrode materials with high capacitance and wide potential windows is central to boost the energy storage performance of ASCs.

Various pseudocapacitive materials have been explored and tested as electrode materials for supercapacitors with special emphasis on transition metal oxides (TMOs) owing to their multiple oxidation states which can result in high capacitance values, excellent energy density, and rapid charge–discharge process [9]. Among several TMOs possessing high capacitance values, namely, RuO_2, MnO_2, ZnO, NiO, Fe_2O_3, and WO_3 [10–12], tungsten oxide is a promising candidate for SCs owing to its versatility, low cost, and multiple oxidation states (+4 to +6) which lead to superior redox pseudocapacitance and electrochemical stability. Despite these advantages, low electrical conductivity and poor cycling stability are the major shortcomings that limit its usage in developing high-performance supercapacitors [13]. Several efforts have been made to overcome these issues by morphological alterations, such as by making nanotubes [14], nanoplates [15], and nanoflowers [16] of tungsten oxides; fabrication of composites like $WO_3@PPy$ [17], WO_3/MnO_2 [18], Graphene-WO_3 hybrids [19]; and insertion of conductive ions in the host matrix, such as WO_3/Se [13]. Another alternative to resolve the aforementioned disadvantages of tungsten oxide is making composites with metal carbides. Transition metal carbides (TMCs) exhibit unique characteristics such as high melting point, corrosion resistance, high hardness, high electrical conductivity, and chemical stability resulting from the coexistence of ionic, covalent, and metallic bonds [20, 21]. Some reports highlight the electrochemical properties of transition metal carbide-based composite materials, such as W_2C:W_xO_y [22] and N-doped $Mo_2C@MoO_3$ [23], but detailed reports on the charge storage mechanism of such composites are scanty.

Inspired by the aforementioned considerations, in this study, we have introduced simple and one-step strategy to synthesize WO_2/W_2C heterostructures by in-situ reduction/carbonization process and have investigated its charge storage mechanism as a supercapacitor electrode in 1 M sodium sulfate aqueous electrolyte. To the best of our knowledge, such a study has not been conducted earlier to explore the charge storage mechanisms in such composites. The electrode material shows excellent electrochemical performance facilitated by mostly surface/near-surface-based fast faradaic reactions. The WO_2/W_2C electrode is also used to realize an ASC which could exhibit a stable voltage window of 1.2 V with an excellent cycling stability.

Experimental section

Synthesis of electrode materials

Tungsten (VI) oxide (WO_3, Sigma-Aldrich, 99.9%) and melamine ($C_3H_6N_6$, Sigma-Aldrich, 99%) were used as precursors to synthesize WO_2/W_2C heterostructures. First, 100 mg WO_3 was grinded with 500 mg melamine in a mortar and pestle. The mixture was then introduced in a fused quartz tube and heated at 800 °C at 5 °C/min for 2 h under argon atmosphere. A possible synthesis mechanism of WO_2/W_2C heterostructures may be stated as follows:

$$WO_3 + C \rightarrow WO_2 \tag{1}$$

$$WO_2 + C \rightarrow W_2C \tag{2}$$

Fabrication of electrodes

For the fabrication of WO_2/W_2C electrodes, active material powder (80 wt%), acetylene black (10 wt%) (Alfa Aesar, $\geq$ 99%), and polyvinylidene fluoride binder (10 wt%) (PVDF, Sigma-Aldrich) were ground and mixed with N-methyl-2-pyrrolidone (NMP) solvent, and then the homogeneous slurry was cast on a Nickel (Ni) foam substrate with an effective surface area of 1 cm^2. The electrodes were dried for 15 h at 80 °C in the oven and pressed at 150 psi pressure for 10 s to get a uniform thin sheet. The loading amount of WO_2/W_2C material on Ni foam substrate was 7.52 mg as calculated by weighing electrodes before and after pasting the slurry.

Structural, morphological, and electrochemical measurement techniques

Morphology and structure of the as-synthesized material were analyzed using field emission scanning electron microscope (FESEM, FEI Nova Nano FESEM450), transmission electron microscope (TEM, Thermofisher, Talos F200S G2), high-resolution TEM (HRTEM), energy dispersive X-ray spectroscopy (EDS), and X-ray diffraction (XRD, PANalytical X-pert PRO diffractometer). Chemical valence states of different constituent elements were investigated using X-ray photoelectron spectroscopy (XPS, ESCA + Omicron Nano Technology) technique. The electrochemical performance of electrodes was explored using an electrochemical workstation (CHI760E) in 1 M sodium sulfate (Na_2SO_4, Qualikems, 99%) electrolyte solution. A standard-three electrode system was used to investigate the electrochemical characteristics of WO_2/W_2C electrode material at room temperature with a Pt wire and Ag/AgCl as counter and reference electrodes,

respectively. The asymmetric supercapacitor was assembled with a polypropylene mesh separator soaked in 1 M Na_2SO_4 electrolyte solution sandwiched between WO_2/W_2C (negative) and activated charcoal (positive electrode). Electrodes were soaked in the electrolyte solution for 3 h prior to electrochemical measurements. The electrochemical behavior and charge storage mechanism is examined via cyclic voltammetry (CV), galvanostatic charge-discharge (GCD), and electrochemical impedance spectroscopy (EIS) tests. CV and GCD behavior were analyzed at various scan rates (10 mV/s to 200 mV/s) and current densities (0.5 mA/cm^2 to 5 mA/cm^2), respectively. EIS measurements were recorded between 100 kHz and 10 mHz frequency loop with 5 mV perturbation amplitude at open circuit potential.

Results and discussion

Morphology and structure of as-synthesized material

A simple, one-step, and scalable strategy is introduced to synthesize WO_2/W_2C heterostructures by in-situ reduction/carbonization process. The synthesis mechanism as per Eqs. (1) and (2) may be stated as follows: Melamine decomposes to form melem between 200–300 °C, and beyond 350 °C melem begins to polymerize to yield g-C_3N_4. It is hypothesized that at higher temperatures (> 600 °C), fragmentation of g-C_3N_4 in gaseous C and N moieties provides a reductive atmosphere resulting in the formation of WO_2 with small amounts of W_2C brought about by further carbonization of the as-formed WO_2. It is to be noted that although we have used melamine as precursor for g-C_3N_4, other substitutes including dicyanamide could also lead to similar final products as observed in our previous studies [24, 25].

As particle size plays a crucial role in providing ample reaction sites during electrochemical reactions, FESEM analyses are carried out to assess the morphology and size of the nanoparticles. In Fig. 1a, the FESEM image of as-synthesized material suggests the presence of polydisperse nanoparticles with sizes varying from 70 to 170 nm. After analyzing a number of such micrographs, the size distribution of these nanoparticles is plotted in Fig. 1b, which suggests the average size of the particles to be 109.5 nm. EDS spectrum (Fig. S1) confirms the presence of W, C, and O as the constituent elements of the as-synthesized material. Figures 1c and S2 demonstrate TEM images of the material, again suggesting polydisperse nature of the particles. In Fig. 1d, e, HRTEM images taken at two different regions (marked as 1 and 2) of Fig. 1c are shown. In Fig. 1d, well-aligned crystalline planes with interplanar spacing of 0.25 nm match well with the spacings of (100) planes in W_2C [26]. Moreover, HRTEM image taken at region 2 of Fig. 1c and

shown in Fig. 1e suggests an interplanar spacing of 0.34 nm which corresponds to the (011) lattice planes in WO_2. In confirmation of HRTEM analyses, different peaks in XRD spectra of the synthesized material, as shown in Fig. 1f, can be indexed perfectly with the reflections for hexagonal W_2C (JCPDS file no.: 01-035-0776) [26] and monoclinic WO_2 (JCPDS file no.: 00-032-1393). Sharp diffraction peaks confirm highly crystalline nature of WO_2 nanoparticles, whereas tiny peaks of W_2C suggest partial carbonization of WO_3 during high-temperature annealing with melamine. Such partial carbonization is advantageous in augmenting the electronic conductivity of oxides-based composites and ameliorating their electrochemical performance.

To have deeper insights on the valence states of constituent elements in as-synthesized material, X-ray photoelectron spectroscopy (XPS) measurements were performed. The survey spectrum (shown in Fig. S3, Supplementary Material) of the WO_2/W_2C composite material verifies the coexistence of constituent elements, namely, W, C, and O, without significant evidence of any impurities. The high-resolution XPS profiles of W 4f, C 1s, and O 1s are displayed in Fig. 1g–i. In the deconvoluted core level XPS spectrum of W 4f presented in Fig. 1g, two peaks at binding energies of 34.4 eV (W 4$f_{5/2}$) and 32.5 eV (W 4$f_{7/2}$) correspond to the W–C bonds in tungsten carbide which is in conformity with literature data as well as the findings from XRD [27]. Other three peaks centered around 38.0, 35.8, and 41.1 eV correspond to the W 4$f_{5/2}$, W 4$f_{7/2}$, and W 5$p_{3/2}$ states of W^{6+} formed superficially due to oxidation at ambient conditions [13, 22, 27]. The XPS spectrum of C 1s can be deconvoluted into three peaks as displayed in Fig. 1h. Stronger peak at 284.6 eV is assigned to C sp^2 hybridized graphitic carbon, whereas smaller peaks at binding energy 285.2 eV and 286.5 eV indicate the presence of C sp^3 corresponding to defects in the system and C sp^2 = O corresponding to the carbon atoms associated with different oxygen-containing groups, respectively [28, 29]. The O 1s spectrum from the WO_2/W_2C composite is also deconvoluted into two peaks as depicted in Fig. 1i. The intense peak located at a lower binding energy of 531 eV can be attributed to the O^{2-} ions, which combine with W cations within the lattice [22]. The second peak at 532.6 eV binding energy can be assigned to the weakly adsorbed oxygen species on the surface (W-OH) [30].

Electrochemical behavior of the material

Electrochemical behavior of the WO_2/W_2C electrode is analyzed using a three-electrode set up with 1 M Na_2SO_4 aqueous electrolyte solution, and test results are depicted in Fig. 2. We have checked the electrochemical performance of WO_2/W_2C electrode in Na_2SO_4 aqueous electrolytes of different concentrations, among which the best electrochemical performance obtained is with 1 M
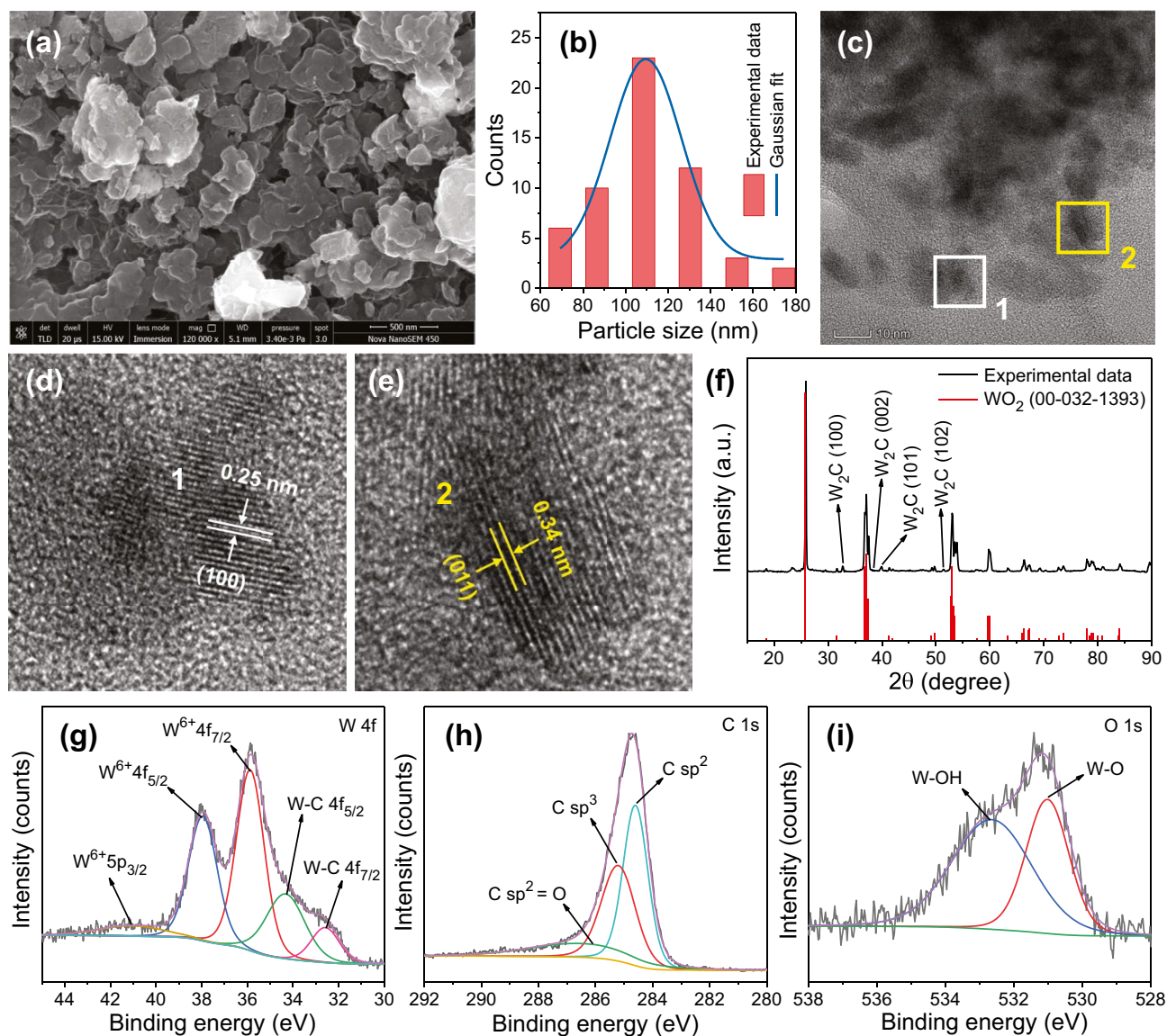
Fig. 1 **a** FESEM image of as-synthesized WO_2/W_2C composite; **b** particle size distribution as measured from a number of FESEM images; **c** TEM image of as-prepared WO_2/W_2C composite; **d,e** HRTEM images showing well aligned lattice planes recorded at the marked regions of **c**; **f** X-ray diffraction pattern of WO_2/W_2C composite; and deconvoluted core level XPS spectra for **g** W 4f, **h** C 1s, and **i** O 1s

Na_2SO_4. Moreover, while testing with KOH as electrolyte, electrode materials were found unstable (material leached out of current collector) at higher current densities and scan rates, resulting inferior electrochemical performance of composite electrode in KOH electrolyte. In general, 1 M Na_2SO_4 (with pH ~ 7) is used as standard aqueous electrolyte to investigate electrochemical performance of various electroactive materials which are not stable in acidic or basic mediums. Such aqueous-based neutral pH electrolytes are promising due to their non-corrosive nature, safety, non-flammability, and better electrochemical stability within a wide potential window as compared to proton

or hydroxide ion containing electrolytes. Moreover, aqueous electrolytes show much higher conductivity as compared to other organic and ionic electrolytes which is beneficial in lowering bulk resistance of the SC device leading to better power delivery [31]. Now, to distinguish between faradaic and non-faradaic charge storage processes, CV measurements were initially performed within the voltage range from −0.3 to −1 V (vs. Ag/AgCl) at various scan rates from 10 to 200 mV/s, and the corresponding voltammograms are shown in Fig. 2a. Good rectangular-shaped CV curve at low scan rates suggests the dominance of electric double-layer capacitance towards overall energy
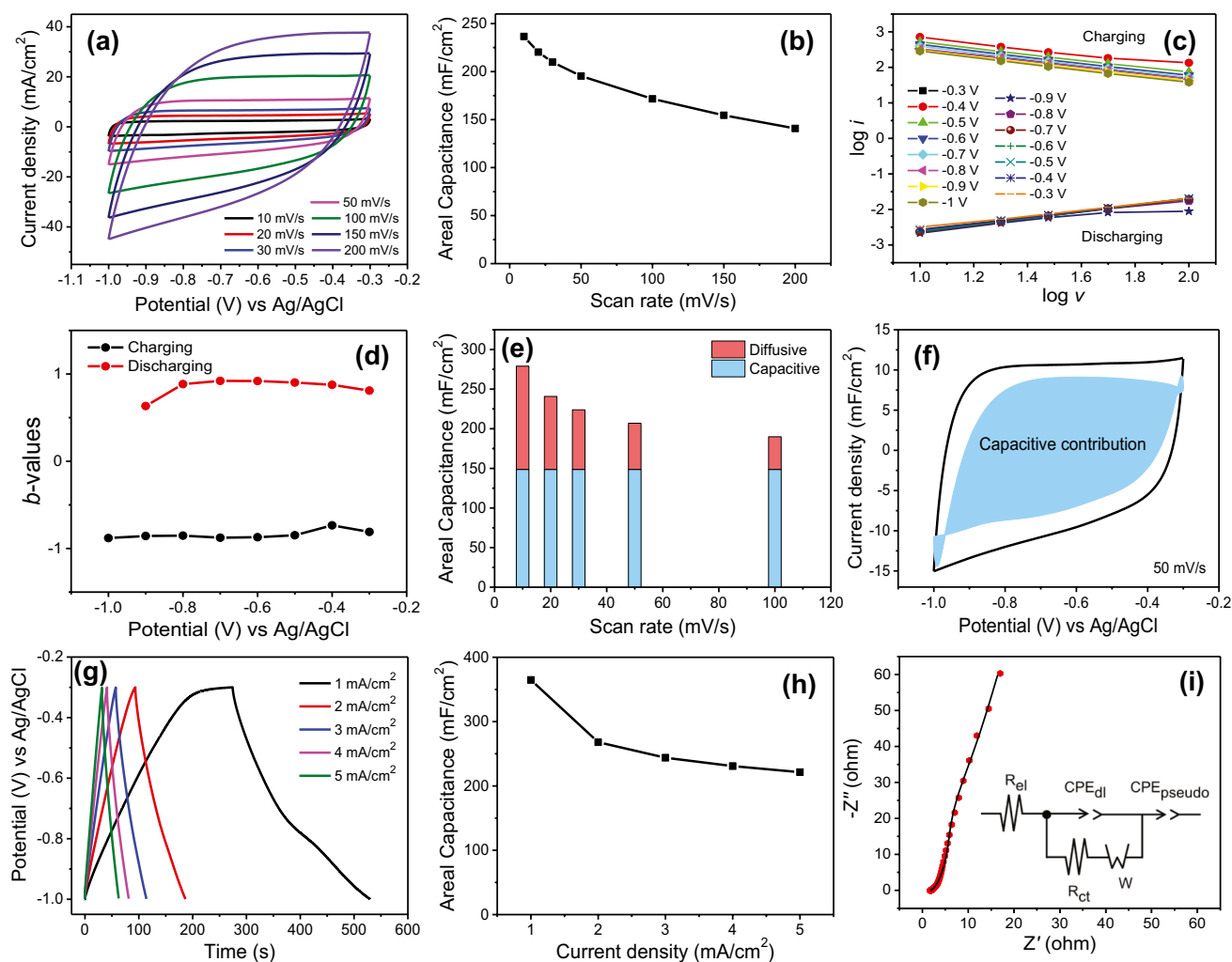
Fig. 2 **a** CV curves of WO_2/W_2C electrode recorded at different scan rates; **b** variation of areal capacitance at different scan rates; **c** log i versus log v plot of WO_2/W_2C electrode at different potentials for charging and discharging; **d** variation of slope "b-values" at different voltages for charging and discharging sweeps of CV; **e** quantitative segregation of capacitive and diffusion-controlled charge storage mechanisms at different scan rates; **f** comparison of capacitive (shaded area) and diffusion-controlled charge storage process at 50 mV/s scan rate for WO_2/W_2C composite electrode; **g** GCD profile of WO_2/W_2C electrode at varying current densities between -0.3 and -1 V (vs. Ag/AgCl); **h** comparison of areal capacitance calculated from discharge step of GCD data; and **i** Nyquist plot of WO_2/W_2C electrode; inset displays the equivalent circuit model to fit Nyquist plot (scattered points are experimental data, whereas the solid line is fitted data)

storage [32]. The quasi-rectangular shapes of CV curves at relatively higher scan rates signify easy charge transfer at the electrode–electrolyte interface and hence suggest its good capacitive behavior [33, 34]. In Fig. 2b, the variation of areal capacitance as calculated from the CVs at different scan rates is plotted against the scan rates. Quantitatively, the composite electrode demonstrates an areal capacitance values of 236.6 mF/cm^2 (31.4 F/g) at 10 mV/s and 140.7 mF/cm^2 (18.7 F/g) at 200 mV/s scan rates. The electrode exhibits capacitance retention of 59.5% as the scan rate increases from 10 to 200 mV/s. Further, in-depth charge storage mechanism and kinetics of WO_2/W_2C electrode are assessed by Dunn's method, which provides relative

contributions of capacitive (EDLC and fast faradaic surface/subsurface redox reactions), and diffusion dominated ion insertion processes (arising from the intercalation/deintercalation of ions in the bulk of electrode material) towards total charge storage [35]. In the scan rate dependent CV measurements, the relation between the current response i(V) with scan rate v can be written as follows:

$$i(V) = av^b \qquad (3)$$

where i(V) is the current in CV, v is scan rate, and a and b are adjustable parameters [36]. The b-values give detailed insights into energy storage behavior, which can be found

from the slopes of log i vs. log v plots at different voltages, as illustrated in Fig. 2c. Particularly, $b = 1$ corresponds to the capacitive process, whereas $b = 0.5$ indicates the diffusion-dominated faradaic process [37]. The b-values obtained in this work are between 0.7 and 0.9 for both cathodic and anodic cycles, as depicted in Fig. 2d, suggesting preferentially capacitive charge storage behavior which can be owed to ample surface redox reactions of WO$_2$/W$_2$C electrode. Now, the percentage contributions of capacitive and diffusive processes towards the total charge stored by the electrode material can be estimated by analysing the current in CVs at different scan rates using following equation:

$$i(V) = a_1 v + a_2 v^{\frac{1}{2}} \tag{4}$$

where i(V) is the current response, v is scan rate, and a_1 and a_2 are adjustable parameters. The terms $a_1 v$ and $a_2 v^{\frac{1}{2}}$ correspond to the capacitive effect (EDLC and surface redox reactions) and diffusion-dominated ion insertion/deinsertion processes, respectively [38]. For ease of calculation, the above equation can be rearranged as follows:

$$i(V)/v^{\frac{1}{2}} = a_1 v^{\frac{1}{2}} + a_2 \tag{5}$$

Therefore, straight lines are obtained by plotting $i(V)/v^{\frac{1}{2}}$ vs. $v^{\frac{1}{2}}$ at various voltages. The values of a_1 and a_2 can be estimated from the slopes and intercepts of the straight lines, respectively, and then the capacitive and diffusive contributions can be segregated quantitatively [39]. In Fig. 2e, we have deduced that the percentage of capacitive contribution for WO$_2$/W$_2$C material is higher (53%) as compared to diffusive contributions (47%) at 10 mV/s scan rate. The analysis further revealed that the percentage of capacitive contribution in WO$_2$/W$_2$C material substantially increases from 53 to 78% with the increase in scan rate from 10 to 100 mV/s (Fig. 2e), suggesting predominant surface redox reactions govern the charge storage behavior at higher scan rates. At 50 mV/s scan rate, ~72% of the total current is capacitive in nature as depicted in Fig. 2f.

Further, galvanostatic charge–discharge curves of WO$_2$/W$_2$C material are recorded within −0.3 to −1 V voltage window at different current densities from 1 to 5 mA/cm^2 as shown in Fig. 2g. A slight deviation from the triangular shape of the charge–discharge curve is observed at lower current density (1 mA/cm^2), which can be attributed to the pseudocapacitance arising out of the redox reactions at the bulk of the electrode at low current densities [40]. The charge–discharge profiles at higher current densities are all symmetric and stable, signifying excellent coulombic efficiency and exemplary capacitive behavior. No sudden voltage drops at the starting of the discharge step are observed which suggests low equivalent series resistance

of the WO$_2$/W$_2$C electrodes [41]. Figure 2h illustrates the areal capacitance vs. current densities plot for WO$_2$/W$_2$C electrode material where the capacitance values are calculated from the discharge steps of the charge–discharge profiles (details in Supplementary Material). The WO$_2$/W$_2$C electrode displays an areal capacitance of 364.7 mF/cm^2 (48.5 F/g) at 1 mA/cm^2 current density. A gradual decrease in capacitance values is observed with the increase in current density from 1 to 5 mA/cm^2, owing to the fact that all the redox-active sites are not accessible to the electrolytic ions at higher current densities [42]. It is very interesting to note that when the current density increases to 5 mA/cm^2, areal capacitance is still maintained at 221.4 mF/cm^2 (29.4 F/g), which is 61% of the areal capacitance delivered at 1 mA/cm^2 current density. The electrochemical performance of WO$_2$/W$_2$C electrode is found to be better than several recently reported electroactive materials (Table S1) [17, 43–46].

Electrochemical impedance spectroscopy (EIS) is performed to evaluate the charge transport properties of the electroactive material. Figures 2i and S4 (Supplementary Material) display the Nyquist plot and Bode plot of WO$_2$/W$_2$C electrode material within 100 kHz to 10 mHz frequency range. The Nyquist plot is composed of two distinct parts: a semicircle in high-frequency region and a sloped line in the low-frequency region. The diameter of the semicircle represents the charge transfer resistance at the interface between electrode and electrolyte; smaller the diameter, lesser the charge transfer resistance for the WO$_2$/W$_2$C material and, hence, better rate capability. Steeper sloped line in the low-frequency region suggests small resistance towards electrolytic ion diffusion and better capacitive behavior [47]. In Fig. 2i, impedance data (scattered points) are fitted (solid lines) with an equivalent Randles circuit shown in the inset of Fig. 2i. The circuit consists of equivalent series resistance (R$_{el}$), charge transfer resistance (R$_{ct}$), constant phase elements (CPEs), and Warburg element (W), and the values of these parameters obtained from Z-View fitting are summarized in Table S2 (Supplementary Material). The low values of R$_{el}$ (1.8 Ω) and R$_{ct}$ (7.7 Ω) signify good conductivity of electrode material and good contact between electrode and electrolyte, facilitating charge transfer kinetics which supports the conclusions drawn from the CV and GCD measurements.

Electrochemical performance evaluation of WO$_2$/W$_2$C//AC ASC

To evaluate practical feasibility of as-synthesized WO$_2$/W$_2$C electrode as high-performance ASC anode, ASC device is assembled using WO$_2$/W$_2$C as a negative electrode and commercial activated charcoal (AC) as positive
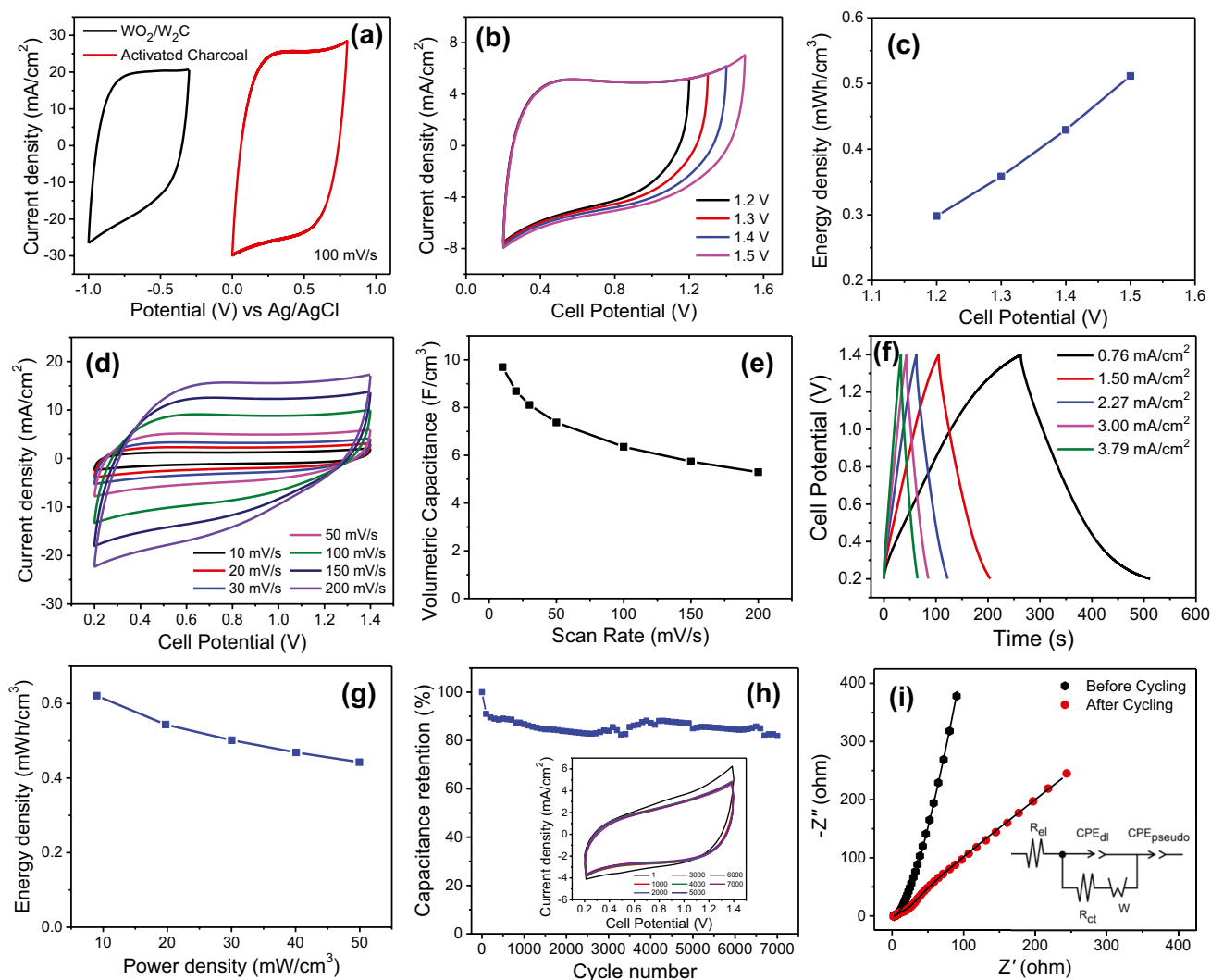
Fig. 3 **a** CV curves of WO$_2$/W$_2$C (anode) and AC (cathode) within their stable operating voltage windows; **b** CV curves of the ASC recorded for different operating potential windows at 50 mV/s scan rate; **c** variation of energy density with operating potential window at 50 mV/s scan rate; **d** CV curves of the ASC at various scan rates; **e** variation of volumetric capacitance with scan rate for the assembled ASC; **f** GCD curves of ASC at varying current densities between 0.2 and 1.4 V; **g** Ragone plot for the ASC; **h** capacitance retention for 7000 CV cycles at the scan rate of 100 mV/s, where inset displays CV curves at different cycles; and **i** Nyquist plots before and after cycling test (scattered points are experimental data whereas solid lines are fitted data), where inset shows the equivalent circuit model to fit Nyquist plots

electrode materials in 1 M Na$_2$SO$_4$ electrolyte. Figure 3a demonstrates stable and compatible potential windows of WO$_2$/W$_2$C (−0.3 to −1 V) and AC (0 to 0.8 V) at 100 mV/s scan rate, which further validates the feasibility of assembling an ASC. Further, a series of CV (Fig. 3b) and charge/discharge measurements (Fig. S5) are performed at 50 mV/s scan rate and 0.76 mA/cm^2 current density, respectively, within various potential windows to estimate the stable and best-operating voltage window of the assembled ASC. From above measurements, it is inferred that the stable voltage window of the designed ASC can be extended up to 0.2-1.4 V only as other side reactions begin to dominate above 1.4 V as can be seen from

Fig. 3b. Figure 3c highlights the enhancement in energy density (calculated according to $E = \frac{1}{2}CV^2$) from 0.3 to 0.5 mWh/cm^3 as operating voltage is increased from 1.2 to 1.5 V. However, due to poor coulombic efficiency at 1.5 V (Fig. S5), 0.2–1.4 V potential window is chosen as the optimum potential window for the ASC for further electrochemical measurements.

Figure 3d displays the CV curves of WO$_2$/W$_2$C//AC ASC between 0.2 and 1.4 V at various scan rates (10 to 200 mV/s) where the quasi-rectangular shape of CVs emphasizes the existence of both double-layer capacitance and pseudocapacitance. With the increase in scan rate from 10 to 200 mV/s, the shape of the CV curves does not change much, indicating

fast charge reaction kinetics of the ASC device. The volumetric capacitances calculated from the CV curves are plotted against scan rate as illustrated in Fig. 3e. The volumetric capacitance of ASC is 9.67 F/cm^3 (~46.2 F/g) at 10 mV/s which retains 56% of the initial capacitance value when scan rate is increased to 200 mV/s. To further estimate the electrochemical performance of the designed ASC, charge/discharge curves are recorded at different current densities as presented in Fig. 3f. The triangular-shaped curves with symmetric charge/discharge steps clearly reveal capacitive behavior congruent with the results obtained in CV. The volumetric capacitance obtained from the discharge step of the GCD curve as a function of current density is plotted in Fig. S6. The ASC delivers a volumetric capacitance of 3.1 F/cm^3 (~15 F/g) at 0.76 mA/cm^2 current density, with an excellent rate capability of 64% when the current density is increased to 3.79 mA/cm^2. Typically, energy density and power density are two crucial factors that assess the energy storage performance and practical applicability of the ASC. The Ragone plot of WO$_2$/W$_2$C//AC ASC, showing the energy-power density values of this device, is presented in Figs. 3g and S7. This device can achieve an energy density of 0.6 mWh/cm^3 at a power density of 9 mW/cm^3 and retain 0.4 mWh/cm^3 energy density at a power density of 50 mW/cm^3, which is much better than recently reported ASC devices in the literatures (Table S1) [17, 43–46]. Figure 3h shows the cycling performance of WO$_2$/W$_2$C//AC ASC measured at 100 mV/s for 7000 cycles. It is noteworthy that the ASC can retain 82% of its initial capacitance value even after 7000 CV cycles. Moreover, quasi-rectangular shape of the CV curves is maintained even after 7000 cycles without any significant change in the loop area (inset of Fig. 3h), suggesting excellent reversibility of electrode reactions and hence superior cycling stability of the ASC device. However, to understand the decrease in capacitance value with cycling, EIS data are recorded before and after cycling studies, and the results are depicted in Figs. 3i and S8. The Nyquist plots (Fig. 3i) are fitted using an equivalent circuit (inset Fig. 3i) to understand the charge storage process comprehensively, and corresponding parameter values are summarized in Table S2. Low values of R$_{el}$ (2.8 Ω) and R$_{ct}$ (3.7 Ω) suggest good electronic conductivity of electrode materials and electrolyte facilitating charge transfer at the electrode/electrolyte interface and charge movement during electrochemical reactions. Minute variation in R$_{el}$ value (2.9 Ω) suggests excellent structural and electrochemical stability of electrode materials during 7000 cycles. However, R$_{ct}$ value changes drastically (81.88 Ω) during cycling tests, representing possible distortions in charge transport pathways due to repetitive ion insertion/de-insertion processes, which in turn leads to capacitance fading during long-term cycling. The Bode plots shown in Fig. S8 further confirm capacitive nature of the ASC with a phase angle of −71.5° at the start of cycling test. The relaxation time constant (τ_0) obtained at −45° phase angle of the assembled ASC device is 0.56 s, revealing its fast charge–discharge characteristics. The relaxation time drops to 0.3 s after 7000 repetitive cycles, representing the degradation of capacitive characteristics with the cycling of ASC.

Conclusion

In summary, we have reported a simple, one-step and scalable strategy to synthesize WO$_2$/W$_2$C heterostructures by in-situ reduction/carbonization process. Partial carbonization of tungsten oxide enhances its electronic conductivity. The electrochemical performance and charge storage mechanism of the as-synthesized WO$_2$/W$_2$C composite material are discussed comprehensively. The contribution from the capacitive and diffusion-dominated charge storage processes are analyzed and quantified from the CV measurements, revealing the dominance of the surface-controlled (capacitive) charge storage processes over diffusion-controlled processes at all scan rates. Besides, the WO$_2$/W$_2$C composite electrode exhibits an excellent areal capacitance value of 364.7 mF/cm^2 at 1 mA/cm^2 current density within −0.3 to −1 V window in 1 M Na$_2$SO$_4$ electrolyte. Further, a novel ASC is assembled with WO$_2$/W$_2$C composite as negative electrode and AC as positive electrode. The ASC WO$_2$/W$_2$C (-)//AC (+) exhibits excellent volumetric capacitance of 9.67 F/cm^3 at 10 mV/s scan rate with good rate capability and superior cycling stability. It can retain 82% of its initial capacitance value even after 7000 CV cycles at 100 mV/s scan rate. The ASC can achieve a maximum energy density of 0.6 mWh/cm^3 at a power density of 9 mW/cm^3. The promising electrochemical properties of WO$_2$/W$_2$C heterostructures synthesized from abundant and low-cost precursors opens up a new avenue for realizing affordable energy storage devices.

References

1. Miller John R, Simon P (2008) Electrochemical capacitors for energy management. Science. https://doi.org/10.1126/science.1158736

2. Simon P, Gogotsi Y (2020) Perspectives for electrochemical capacitors and related devices. Nat Mater. https://doi.org/10.1038/s41563-020-0747-z

3. Chen Z, Qin Y, Weng D, Xiao Q, Peng Y, Wang X, Li H, Wei F, Lu Y (2009) Design and synthesis of hierarchical nanowire

composites for electrochemical energy storage. Adv Funct Mater. https://doi.org/10.1002/adfm.200900971

4. Mai L-Q, Yang F, Zhao Y-L, Xu X, Xu L, Luo Y-Z (2011) Hierarchical MnMoO$_4$/CoMoO$_4$ heterostructured nanowires with enhanced supercapacitor performance. Nat Commun. https://doi.org/10.1038/ncomms1387

5. Wang Y, Xia Y (2013) Recent progress in supercapacitors: from materials design to system construction. Adv Mater. https://doi.org/10.1002/adma.201301932

6. Yan J, Wang Q, Wei T, Fan Z (2014) Recent advances in design and fabrication of electrochemical supercapacitors with high energy densities. Adv Energy Mater. https://doi.org/10.1002/aenm.201300816

7. Wang G, Zhang L, Zhang J (2012) A review of electrode materials for electrochemical supercapacitors. Chem Soc Rev. https://doi.org/10.1039/C1CS15060J

8. Shao Y, El-Kady MF, Sun J, Li Y, Zhang Q, Zhu M, Wang H, Dunn B, Kaner RB (2018) Design and mechanisms of asymmetric supercapacitors. Chem Rev. https://doi.org/10.1021/acs.chemrev.8b00252

9. Kumar A, Rathore HK, Sarkar D, Shukla A (2021) Nanoarchitectured transition metal oxides and their composites for supercapacitors. Electrochem Sci Adv. https://doi.org/10.1002/elsa.202100187

10. Mohd Abdah MAA, Azman NHN, Kulandaivalu S, Sulaiman Y (2020) Review of the use of transition-metal-oxide and conducting polymer-based fibres for high-performance supercapacitors. Mater Des. https://doi.org/10.1016/j.matdes.2019.108199

11. Shinde PA, Jun SC (2020) Review on recent progress in the development of tungsten oxide based electrodes for electrochemical energy storage. Chemsuschem. https://doi.org/10.1002/cssc.201902071

12. Zhang G, Xiao X, Li B, Gu P, Xue H, Pang H (2017) Transition metal oxides with one-dimensional/one-dimensional-analogue nanostructures for advanced supercapacitors. J Mater Chem A. https://doi.org/10.1039/C7TA02454A

13. Barik R, Yadav AK, Jha SN, Bhattacharyya D, Ingole PP (2021) Two-dimensional tungsten oxide/selenium nanocomposite fabricated for flexible supercapacitors with higher operational voltage and their charge storage mechanism. ACS Appl Mater Interfaces. https://doi.org/10.1021/acsami.0c15818

14. Shinde PA, Seo Y, Ray C, Jun SC (2019) Direct growth of WO$_3$ nanostructures on multi-walled carbon nanotubes for high-performance flexible all-solid-state asymmetric supercapacitor. Electrochim Acta. https://doi.org/10.1016/j.electacta.2019.03.159

15. Huang Y, Li Y, Zhang G, Liu W, Li D, Chen R, Zheng F, Ni H (2019) Simple synthesis of 1D, 2D and 3D WO$_3$ nanostructures on stainless steel substrate for high-performance supercapacitors. J Alloys Compd. https://doi.org/10.1016/j.jallcom.2018.11.212

16. Qiu M, Sun P, Shen L, Wang K, Song S, Yu X, Tan S, Zhao C, Mai W (2016) WO$_3$ nanoflowers with excellent pseudo-capacitive performance and the capacitance contribution analysis. J Mater Chem A. https://doi.org/10.1039/C6TA00237D

17. Wang F, Zhan X, Cheng Z, Wang Z, Wang Q, Xu K, Safdar M, He J (2015) Tungsten oxide@ polypyrrole core–shell nanowire arrays as novel negative electrodes for asymmetric supercapacitors. Small. https://doi.org/10.1002/smll.201402340

18. Sarkar D, Mukherjee S, Pal S, Sarma DD, Shukla A (2018) Hexagonal WO$_3$ nanorods as ambipolar electrode material in asymmetric WO$_3$//WO$_3$/MnO$_2$ supercapacitor. J Electrochem Soc. https://doi.org/10.1149/2.0451810jes

19. Xing L-L, Huang K-J, Fang L-X (2016) Preparation of layered graphene and tungsten oxide hybrids for enhanced performance supercapacitors. Dalton Trans. https://doi.org/10.1039/C6DT03719D

20. Zhang H, Liu J, Tian Z, Ye Y, Cai Y, Liang C, Terabe K (2016) A general strategy toward transition metal carbide/carbon core/shell nanospheres and their application for supercapacitor electrode. Carbon. https://doi.org/10.1016/j.carbon.2016.01.047

21. Zhong Y, Xia X, Shi F, Zhan J, Tu J, Fan HJ (2016) Transition metal carbides and nitrides in energy storage and conversion. Adv Sci. https://doi.org/10.1002/advs.201500286

22. Soares DM, Vicentini R, Peterlevitz AC, Rodella CB, da Silva LM, Zanin H (2019) Tungsten oxide and carbide composite synthesized by hot filament chemical deposition as electrodes in aqueous-based electrochemical capacitors. J Energy Storage. https://doi.org/10.1016/j.est.2019.100905

23. Cevik E, Gunday ST, Iqbal A, Akhtar S, Bozkurt A (2022) Synthesis of hierarchical multilayer N-doped Mo$_2$C@MoO$_3$ nanostructure for high-performance supercapacitor application. J Energy Storage. https://doi.org/10.1016/j.est.2021.103824

24. Das D, Das A, Reghunath M, Nanda KK (2017) Phosphine-free avenue to Co$_2$P nanoparticle encapsulated N, P co-doped CNTs: a novel non-enzymatic glucose sensor and an efficient electrocatalyst for oxygen evolution reaction. Green Chem. https://doi.org/10.1039/C7GC00084G

25. Das D, Santra S, Nanda KK (2018) In situ fabrication of a nickel/molybdenum carbide-anchored N-doped graphene/CNT hybrid: an efficient (pre)catalyst for OER and HER. ACS Appl Mater Interfaces. https://doi.org/10.1021/acsami.8b09941

26. Lewandowski M, Szymańska-Kolasa A, Sayag C, Beaunier P, Djéga-Mariadassou G (2014) Atomic level characterization and sulfur resistance of unsupported W$_2$C during dibenzothiophene hydrodesulfurization. Classical kinetic simulation of the reaction. Appl Catal B: Environ. https://doi.org/10.1016/j.apcatb.2013.08.011

27. Stellwagen DR, Bitter JH (2015) Structure–performance relations of molybdenum- and tungsten carbide catalysts for deoxygenation. Green Chem. https://doi.org/10.1039/C4GC01831A

28. Kumar A, Sarkar D, Mukherjee S, Patil S, Sarma DD, Shukla A (2018) Realizing an asymmetric supercapacitor employing carbon nanotubes anchored to Mn$_3$O$_4$ cathode and Fe$_3$O$_4$ anode. ACS Appl Mater Interfaces. https://doi.org/10.1021/acsami.8b16639

29. Lesiak B, Kövér L, Tóth J, Zemek J, Jiricek P, Kromka A, Rangam N (2018) C sp^2/sp^3 hybridisations in carbon nanomaterials – XPS and (X)AES study. Appl Surf Sci. https://doi.org/10.1016/j.apsusc.2018.04.269

30. Vasilopoulou M, Soultati A, Georgiadou DG, Stergiopoulos T, Palilis LC, Kennou S, Stathopoulos NA, Davazoglou D, Argitis P (2014) Hydrogenated under-stoichiometric tungsten oxide anode interlayers for efficient and stable organic photovoltaics. J Mater Chem A. https://doi.org/10.1039/C3TA13975A

31. Pal B, Yang S, Ramesh S, Thangadurai V, Jose R (2019) Electrolyte selection for supercapacitive devices: a critical review. Nanoscale Adv. https://doi.org/10.1039/C9NA00374F

32. Jana M, Saha S, Khanra P, Samanta P, Koo H, Chandra Murmu N, Kuila T (2015) Non-covalent functionalization of reduced graphene oxide using sulfanilic acid azocromotrop and its application as a supercapacitor electrode material. J Mater Chem A. https://doi.org/10.1039/C4TA07009G

33. Chen P-C, Shen G, Shi Y, Chen H, Zhou C (2010) Preparation and characterization of flexible asymmetric supercapacitors based on transition-metal-oxide nanowire/single-walled carbon nanotube hybrid thin-film electrodes. ACS Nano. https://doi.org/10.1021/nn100856y

34. Dong X, Jin H, Wang R, Zhang J, Feng X, Yan C, Chen S, Wang S, Wang J, Lu J (2018) High volumetric capacitance, ultralong life supercapacitors enabled by Waxberry-derived hierarchical porous carbon materials. Adv Energy Mater. https://doi.org/10.1002/aenm.201702695

35. Huang Z-H, Song Y, Feng D-Y, Sun Z, Sun X, Liu X-X (2018) High mass loading MnO$_2$ with hierarchical nanostructures for supercapacitors. ACS Nano. https://doi.org/10.1021/acsnano.8b00621

36. Iamprasertkun P, Tanggarnjanavalukul C, Krittayavathananon A, Khuntilo J, Chanlek N, Kidkhunthod P, Sawangphruk M (2017) Insight into charge storage mechanisms of layered MnO$_2$ nanosheets for supercapacitor electrodes: in situ electrochemical X-ray absorption spectroscopy. Electrochim Acta. https://doi.org/10.1016/j.electacta.2017.08.002

37. Sarkar D, Das D, Das S, Kumar A, Patil S, Nanda KK, Sarma DD, Shukla A (2019) Expanding interlayer spacing in MoS$_2$ for realizing an advanced supercapacitor. ACS Energy Lett. https://doi.org/10.1021/acsenergylett.9b00983

38. Hwang S-K, Patil SJ, Chodankar NR, Huh YS, Han Y-K (2022) An aqueous high-performance hybrid supercapacitor with MXene and polyoxometalates electrodes. Chem Eng J. https://doi.org/10.1016/j.cej.2021.131854

39. Zhu Y, Peng L, Chen D, Yu G (2016) Intercalation pseudocapacitance in ultrathin VOPO$_4$ nanosheets: toward high-rate alkali-ion-based electrochemical energy storage. Nano Lett. https://doi.org/10.1021/acs.nanolett.5b04610

40. Chidembo AT, Aboutalebi SH, Konstantinov K, Jafta CJ, Liu HK, Ozoemena KI (2014) In situ engineering of urchin-like reduced graphene oxide–Mn$_2$O$_3$–Mn$_3$O$_4$ nanostructures for supercapacitors. RSC Adv. https://doi.org/10.1039/C3RA44973D

41. Liang J, Chen S, Xie M, Wang Y, Guo X, Guo X, Ding W (2014) Expeditious fabrication of flower-like hierarchical mesoporous carbon superstructures as supercapacitor electrode materials. J Mater Chem A. https://doi.org/10.1039/C4TA03209H

42. Kandambeth S, Jia J, Wu H, Kale VS, Parvatkar PT, Czaban-Jóźwiak J, Zhou S, Xu X, Ameur ZO, Abou-Hamad E (2020) Covalent organic frameworks as negative electrodes for high-performance asymmetric supercapacitors. Adv Energy Mater. https://doi.org/10.1002/aenm.202001673

43. Mao N, Chen W, Meng J, Li Y, Zhang K, Qin X, Zhang H, Zhang C, Qiu Y, Wang S (2018) Enhanced electrochemical properties of hierarchically sheath-core aligned carbon nanofibers coated carbon fiber yarn electrode-based supercapacitor via polyaniline nanowire array modification. J Power Sources. https://doi.org/10.1016/j.jpowsour.2018.07.022

44. Veerasubramani GK, Krishnamoorthy K, Pazhamalai P, Kim SJ (2016) Enhanced electrochemical performances of graphene based solid-state flexible cable type supercapacitor using redox mediated polymer gel electrolyte. Carbon. https://doi.org/10.1016/j.carbon.2016.05.008

45. Wang S, Zhu J, Shao Y, Li W, Wu Y, Zhang L, Hao X (2017) Three-dimensional MoS$_2$@ CNT/RGO network composites for high-performance flexible supercapacitors. Chem Eur J. https://doi.org/10.1002/chem.201605465

46. Zhou J, Chen N, Ge Y, Zhu H, Feng X, Liu R, Ma Y, Wang L, Hou W (2018) Flexible all-solid-state micro-supercapacitor based on Ni fiber electrode coated with MnO$_2$ and reduced graphene oxide via electrochemical deposition. Sci China Mater. https://doi.org/10.1007/s40843-017-9168-9

47. Ali GAM, Fouad OA, Makhlouf SA, Yusoff MM, Chong KF (2014) Co$_3$O$_4$/SiO$_2$ nanocomposites for supercapacitor application. J Solid State Electrochem. https://doi.org/10.1007/s10008-014-2510-3

Publisher's Note Springer Nature remains neutral with regard to jurisdictional claims in published maps and institutional affiliations.